The Effects of Transition Metal Oxide Doping on the Sintering of Cerium Gadolinium Oxide

Samuel Taub [a], Robert E. A. Williams [b], Xin Wang [a], David W. McComb [b], John A. Kilner [a] and Alan Atkinson [a]

[a] Department of Materials, Imperial College, London, SW7 2AZ, U.K.

[b] Center for Electron Microscopy and Analysis, Department of Materials Science and Engineering, The Ohio State University, Columbus, OH 43212, U.S.A.

E-mail Addresses

Samuel Taub: samuel.taub@imperial.ac.uk

Robert E. A. Williams: rowilli8@vt.edu

Xin Wang: xin.wang@imperial.ac.uk

David W. McComb: mccomb.29@osu.edu

John A. Kilner: j.kilner@imperial.ac.uk

Alan Atkinson: alan.atkinson@imperial.ac.uk

Corresponding Author

Professor Alan Atkinson (alan.atkinson@imperial.ac.uk)

Imperial College London, Department of Materials, Royal School of Mines, Prince Consort Road, South Kensington, London, SW7 2BP, United Kingdom.

Telephone: +44 (0) 207 594 6780

Abstract

The effects of two transition metal oxide dopants, Co and Cr, on the densification properties of $Ce_{0.9}Gd_{0.1}O_{1.95}$ (CGO) have been examined. Whilst low concentration Co oxide was found to reduce the sintering temperature of CGO by over 150 °C, the addition of Cr oxide, at concentrations greater than 0.1 cat %, was found to be detrimental to the densification of the material. EDX spectrum imaging was used to examine the elemental evolution in both materials. At approximately 70 % relative density, a continuous TMO rich film was located around the primary crystallites in both materials. With increasing relative density, the concentration of both dopants was shown to decrease without there being considerable change in the apparent grain boundary layer thicknesses. All specimens examined revealed considerable grain boundary Gd enrichment and Ce depletion, with this effect becoming more pronounced with increasing relative density in the Cr-doped CGO. EDX spectrum imaging performed on the high density specimens revealed the presence of discrete second phases in both materials which were subsequently analysed by EELS. Using the current set of results, mechanisms responsible for the modified densification behaviour in Co-doped and Cr-doped CGO are suggested.

Keywords: Cerium Gadolinium Oxide, Transition Metal Oxide Doping, Grain Boundary Segregation, EDX Spectrum Imaging, Sintering

1. Introduction

Doped cerium oxides are promising candidates for solid oxide fuel cell (SOFC) electrolytes operating within the intermediate temperature range (500-700°C), having been shown to exhibit ionic conductivities superior to those of conventional zirconia solid solutions [1, 2]. In

particular, 10 cat % gadolinium doped ceria, $Ce_{0.9}Gd_{0.1}O_{1.95}$ (CGO), has shown potential as an effective electrolyte material, having exhibited some of the highest conductivities amongst the lanthanide dopants in ceria [3, 4]. Intermediate temperature operation is beneficial, in part, as it facilitates the use of cheaper and more robust stainless steel interconnects and cell supports. However, CGO powders typically require sintering temperatures in excess of 1300 °C for full densification [5, 6] which makes the co-firing of the electrolyte and stainless steel supports difficult due to degradation of the stainless steel at temperatures above approximately 1000 °C.

A reduction in the sintering temperature of CGO can be achieved in one of several ways; these include the use of less conventional synthesis routes that will result in the formation of a nanometric scale powder [7-9]. Such powders will promote densification at lower temperatures by increasing the driving force for densification and reducing the distances over which matter must be transported [10]. Novel sintering processes, such as the application of an electric field, have also been shown to reduce the sintering temperature of CGO [11], but are difficult to implement in manufacturing cells. An alternative and more practical approach is to introduce a sintering aid. Doping CGO with the transition metal oxides (TMOs) of Co, Cu, Mn, Ni and Fe have all been shown to improve the densification behaviour of the material when added at low concentrations (typically 1-2 cat %) [6, 12-15]. In particular, low concentration CoO-doping has proved to be an effective sintering aid without having a deleterious effect on the conductivity [16, 17]. Kleinlogel *et al*. [12] reported that 1-5 cat % CoO reduced the temperature required to fully densify $Ce_{0.8}Gd_{0.2}O_{1.9}$ (CGO20) to below 900 °C. These findings are in good agreement with those of Lewis *et al*. [18] who concluded that 2 cat % Co was the most effective dopant concentration. The improved densification kinetics associated with TMO-doping have previously been attributed to a variety of mechanisms. In the case of Co, it was suggested that an amorphous Co-rich

grain boundary film is formed that facilitates densification via liquid phase sintering [13]. This however infers the presence of a liquid phase well below the eutectic temperature of the CeO_2-CoO system. Ivas *et al*. [19] estimated that the liquidus temperature in this system would be lowered from 1644 °C in bulk materials to 1327 °C for 5 nm diameter nano-particles. They applied this to a sintering model and concluded that for a typical addition to ceria of 1 cat % CoO, a 1 nm thick eutectic film would form at particle contacts having a eutectic temperature of 1180 °C which is close to, although still somewhat higher than, the densification onset temperature observed experimentally.

On the other hand, Zhang *et al*. [20] concluded, based on the sintering kinetics, that Fe-doping led to the activation of an early stage viscous flow sintering mechanism in CeO_2, which enhanced densification by increasing the particle contact area, leading to an increased diffusion flux. This concept was also used by the same authors to explain the improved densification behaviour they observed in Co-doped [21] and Mn-doped [6] CGO20.

As well as deliberately adding TMOs as sintering aids, the use of stainless steel in a metal supported cell could potentially lead to elements from the steel (particularly Cr) entering the electrolyte during manufacture. The incorporation of such impurity TMOs has previously been shown to be detrimental to the sinterability of the material [22].

Variations in the resulting microstructures have also been reported. Whilst Jud *et al*. [23] observed a Co containing grain boundary layer in 5 cat % Co doped CGO, Avila-Paredes *et al*. [24], who studied TMO-doped (Fe, Co, Mn and Cu) CGO using electron energy loss spectroscopy (EELS), reported no evidence of a second phase along the grain boundaries. Zhang *et al*. [25] noted the presence of Co-rich precipitates at the triple grain junctions of high density Co-doped CGO20 using high resolution transition electron microscopy (HR-TEM), in agreement with Zając *et al*. [26] who reported the presence of TMO-rich second

phases in Cr, Fe, Ni and Cu-doped $Ce_{0.85}Gd_{0.15}O_{1.925}$ (CGO15) using synchrotron X-ray powder diffraction (SXRD). These elemental analyses were, however, all performed on specimens sintered to high density and as such provided no information as to the location or concentration (and hence possible role) of the TMOs during the densification process. It is therefore likely that the mechanisms outlined above, in relation to the modified sintering behaviour, may have been prematurely assessed and that further examination of these materials is required as a function of relative density.

In this current work, the effects of two contrasting TMO dopants (Co, a known sintering aid, and Cr, a known sintering inhibitor) on the densification of CGO have been examined. The location and concentration of these dopants has also been studied as a function of relative density using energy dispersive X-ray (EDX) spectrum imaging. In light of these findings, the roles these dopants play in the densification of CGO have been reassessed and alternative mechanisms suggested for the modified sintering behaviour.

2. Experimental Procedure

Commercially available $Ce_{0.9}Gd_{0.1}O_{1.95}$ (CGO) powder (NexTech Materials, Ohio, USA) with a specific surface area of 31 $m^2\ g^{-1}$ and average crystallite size of 36 nm was used as the starting material, to which the appropriate transition metal dopants were added in the form of nitrates ($Co(NO_3)_2{\cdot}6H_2O$ and $Cr(NO_3)_3{\cdot}9H_2O$, Alfa Aesar, Lancashire, UK). The selected dopant concentrations were achieved by mixing the required stoichiometric quantities of CGO powder and a solution of transition metal nitrate in ethanol (1 ml per gram of CGO) and stirring thoroughly for 30 minutes in an agate mortar. The slurries were then oven dried at 70 °C for a minimum of 4 hours allowing the ethanol to evaporate after which the mixtures were re-ground. The resulting powders were subsequently calcined in air for 1 hour at 650 °C. The experimental procedure was repeated for the as-received CGO powder, but without the

addition of the transition metal nitrates to provide a TMO-free reference. To prevent delamination when pressing pellets, it was found necessary to increase the powder agglomerate size. This was achieved by isostatically pressing the powders at 120 MPa, re-grinding them in an agate mortar and then passing them through a 38 μm stainless steel mesh. All agglomerated powders were then uniaxially pressed at 75 MPa for 15 s in a cylindrical stainless steel die before being isostatically pressed at 300 MPa for 30 s. Green body densities were measured geometrically, whereas sintered body densities were measured by the Archimedes method using theoretical densities determined by Rietveld refinement of X-ray diffractograms. The sintering behaviour of the pellets was determined using constant heating rate dilatometry (Type 402C, Netzsch-Gerätebau GmbH, Selb, Germany) in laboratory air followed by furnace cooling. TEM cross-sections were prepared from sintered, bulk specimens using a focused ion beam (FIB) milling system (Helios NanoLab, FEI, Eindhoven, The Netherlands). A gold coating (~20 nm) was deposited onto the surface of the sintered pellets by sputter deposition prior to milling to prevent charging of the samples. TEM cross-sections were milled at 30 kV using a Ga-ion beam and thinned to electron transparency at 2 kV. Conventional bright-field TEM was performed at an accelerating voltage of 200 kV (JEM-2000FX Transmission Electron Microscope, JEOL Ltd., Tokyo, Japan).

STEM imaging and subsequent EDX spectrum imaging were performed using a Titan^{3TM} 60-300 (FEI Company, U.S.A.) equipped with a high coherence, high brightness, field emission electron gun (X-FEG), C_s-image corrector and an electron gun monochromator to provide useable probe current with an energy resolution of 0.15 eV collected using a Gatan Enfina spectrometer which produces high-speed spectral maps from electron energy loss spectroscopy (EELS) data. The system is also equipped with a high-speed, high-throughput, quad-silicon drift detector (Super-X), optimised for rapid X-ray collection. All post-processing X-ray analysis was performed using Esprit v1.9 (Bruker Nano GmbH, Berlin,

Germany). The STEM/EDX analyses were performed at an electron beam energy of 300 keV and current of 600-800 nA. The incident spot size was estimated to be 0.15-0.18 nm and the specimen thickness at the analysed region was estimated from the zero energy loss current to be typically 60-100 nm.

3. Results and Discussion

3.1 Sintering Studies

The effect of low concentration Co-doping on the densification and shrinkage rate of CGO in constant heating rate dilatometry is shown in **Figure 1**. Based on previous literature findings [12, 23, 27], a dopant concentration of 2 cat % Co (2CoCGO) has been used to examine the densification behaviour of the material. With reference to **Figure 1**, the addition of Co is shown to enhance the sinterability of the undoped material by reducing both the final sintering temperature and increasing the magnitude of the final shrinkage, whilst the temperature corresponding to the maximum shrinkage rate is also shifted to lower temperature (~900 ºC). At a heating rate of 10 °C min^{-1}, a relative density of 98 % was attained in 2CoCGO below 1100 °C, whereas in the Co-free material this density could only be achieved at 1250 °C, indicating a reduction in sintering temperature of over 150 °C. In a separate experiment, a relative density >99 % was attainable in 2CoCGO after sintering at 1020 °C for 45 min. These results are in good agreement with the literature for both CGO [23] and CGO20 [12]. A decrease in green density is also observed in **Figure 1** for 2CoCGO. This difference is thought to result from the Co modifying the inter-particle forces, leading to a less favourable packing geometry. Jud *et al*. [27] noted a correlation between dopant concentration and sintering onset temperature in their study of Co-doped CGO20, suggesting

that a lower packing density would result in a longer first stage sintering regime. The introduction of Co-oxide as a sintering aid is also shown to reduce the temperature range over which densification occurs. Whilst CGO exhibits a broad sintering range of ~400 °C, 2CoCGO had completed the densification process within ~200 °C. This decrease is however not as pronounced as that reported by Kleinlogel *et al*. [13] in Co-doped CGO20, where the densification process was noted to have reached completion within 50 °C.

The effects of low concentration Cr-doping on the densification behaviour of CGO are shown in **Figure 2**. It is apparent from the figure that Cr-concentrations in excess of 0.1 cat % (0.1CrCGO) inhibit the sintering kinetics compared to the undoped material (**Figure 2a**), with this effect becoming more pronounced with increasing dopant concentration. For dopant levels above 0.5 cat %, final stage sintering had yet to be reached even at 1300 °C. Archimedes measurements on the sintered products showed that relative densities greater than 96 % could only be achieved in all powder compositions after sintering at 1500 °C for 5 hours. These results are in partial agreement with those of Zając *et al*. [26] who observed an increase in the temperature of maximum shrinkage, T_{max}, with increasing Cr content for CGO15, although they described Cr doping as being ineffective as opposed to detrimental to the densification. It is interesting to note that Cr appears to be the only transition metal oxide studied in the literature that has not proved beneficial to the sinterability of CGO. The densification curves of 0.5CrCGO, 1CrCGO and 2CrCGO also appear to show slight inflections during intermediate stage sintering. **Figure 2b** shows the relative linear shrinkage rates as a function of temperature for the different Cr concentrations. The linear shrinkage rate curves of 0.001CrCGO, 0.01CrCGO and 0.1CrCGO exhibit single maxima (as was the case for CGO and 2CoCGO), whereas the curves pertaining to Cr concentrations of 0.5-2 cat % show two maxima, the first of which corresponds well to the onset of the aforementioned inflection points in **Figure 2a**. It is strange to note however, that the temperatures of these

inflection points do not correlate with increasing dopant concentration. Subsequent EDX spectrum imaging experiments of 2CrCGO (see later) did however reveal the formation of a Cr-rich second phase that may explain these changes in densification behaviour. Full analysis of the microstructural evolution is given in the ensuing sections.

The apparent sintering activation energy was determined as a function of relative density for samples of CGO, 2CoCGO and 2CrCGO based on constant heating rate dilatometry performed at heating rates of 3, 5, 10, 20 and 30 °C min^{-1}. The relative linear shrinkage measured at any given temperature, T, was converted into relative density, ρ, assuming isotropic shrinkage:

$$\rho = \rho_0 \left(1 + \frac{\Delta L}{L_0}\right)^3 \quad (1)$$

where ρ_0 is the green density, ΔL is the uniaxial shrinkage and L_0 is the initial sample length. The apparent sintering activation energy at any given density was determined from the gradient of $\ln(d\rho/dt)$ against $1/T$. The results are shown in **Figure 3** for relative densities ranging from 65-85 % for all materials studied. A comparison of the plots reveals notable differences in the evolution of the apparent sintering activation energy for the different materials. A steady increase in apparent activation energy is noted for undoped CGO with density, whereas a decrease in apparent activation energy is observed for the Co-doped material across the same density range. These findings are in good agreement with those of Jud *et al*. [27] who compared the apparent activation energy of CGO20 and CGO20 + 1 cat% Co (1CoCGO20) using a combined-stage sintering model that assumed constant grain size. An increase from approximately 340 to 630 kJ mol^{-1} was reported for the undoped material whereas a decrease from approximately 530 to 430 kJ mol^{-1} was reported for the doped material between relative densities of 65 and 85 %. Values of the activation energy in the

present study were found to increase from 425 to 645 kJ mol^{-1} for CGO and decrease from 500 to 405 kJ mol^{-1} for 2CoCGO. The apparent sintering activation energy of 2CoCGO is significantly lower than that of the undoped material for relative densities greater than about 70 %. A large increase in apparent activation energy is however observed for 2CrCGO, with values in excess of 3000 kJ mol^{-1} recorded at the higher relative densities. The magnitudes of these apparent activation energies are interesting since they highlight possible flaws made in the assumptions underlying their derivation. Higher apparent activation energy values are however expected for Cr-doped CGO due to the noticeable retardation of the sintering kinetics observed in the dilatometry data (**Figure 2a).** It is important to note that the activation energies determined in this study have been termed *apparent*, since any calculations based on dilatometry data require that the microstructure is only a function of the density, and this is not generally valid. For example, in the case of CGO20, Jud *et al*. [27] concluded, based on diffusion coefficient measurements, that surface diffusion would be the dominant transport pathway in early stage sintering. Surface diffusion is known to have a lower activation energy than grain boundary diffusion and is therefore likely to be preferred at lower temperatures. Surface diffusion leads to particle neck formation, but does not contribute towards densification as measured by dilatometry. It does however result in a reduction in the driving force for densification since there is a reduced total surface area. As a result, in this example, the densification rate at low temperatures would be slower than expected, leading to a higher apparent sintering activation energy. In the later stages of sintering, grain growth can have a distorting influence on the apparent activation energy for sintering if the activation energy for grain growth is different from that of the dominant sintering transport mechanism (e.g. grain boundary diffusion). Nevertheless, despite these uncertainties in the absolute values of the activation energy, it is clear that the 2CrCGO has a significantly increased activation energy for densification when compared to the other

materials and although it cannot be stated unequivocally, it is suggested on this basis that Co will probably increase the rate of grain boundary transport whilst Cr will decrease it.

Figure 4 shows bright-field TEM micrographs of CGO, 2CoCGO and 2CrCGO sintered to 932 °C at heating rates of 10 °C min^{-1}. This sintering temperature was chosen so that neck development would still be observable in 2CoCGO and also that a density sufficient for TEM sample lift-out would be achieved in 2CrCGO. The relative densities of the samples were measured by the Archimedes method as approximately 69 %, 87 % and 60 % respectively. The figure indicates that neck formation had initiated in all three materials at 932 °C. It is also clear that Co-doping increases the rate of grain growth in CGO, presumably due to the higher density of 2CoCGO leading to less grain boundary pinning by the pores, whilst Cr-doping appears to have little effect.

3.2 Dopant Distribution as a Function of Density

The sintering behaviour of TMO-doped CGO may be better understood by examining the changes in the grain boundary chemistry using TEM with elemental analysis. Most of the published work on this topic has so far focused on fully dense microstructures which do not provide direct information relating to how the TMOs may have influenced the densification process. Therefore the evolution of grain boundary chemistry was investigated as a function of relative density for samples of 2CoCGO and 2CrCGO using STEM with fully quantifiable EDX spectrum imaging. Samples with relative densities of 70 %, 80 % and 90 % were chosen for evaluation together with samples sintered to maximum density. The measured densities, as determined by the Archimedes method, are shown in **Table 1**. For convenience, the samples will be referred to by their intended densities. All dopant concentrations are

given in *normalised* mass %, where the concentrations of Ga, Cu, Au and Pt (resulting from sample preparation) have been subtracted prior to quantification.

3.2.1 Co-dopant Distribution as a Function of Density

The location and concentration of the Co-oxide dopant between approximately 70 % ($2CoCGO_{70\%}$) and 90 % relative density ($2CoCGO_{90\%}$) is shown in **Figure 5**. At ~70 % relative density (**Figures 5a-b**), noticeable Co enrichment is observed around the primary CGO crystallite grain boundaries and around the edges of pores (which could be an artefact of the technique).

After initial doping, the Co-nitrate is expected to be located on the outer surfaces of the particle agglomerates and then during calcination diffuses into the agglomerates along the grain boundaries to form a Co oxide grain boundary film around the primary particle crystallites. Kleinlogel *et al*. [12] observed a similar Co-rich grain boundary film in 1CoCGO20 when sintering was interrupted at 900 °C after 10 minutes (at a relative density of ~70 %). In that study, the Co-rich film was clearly located around the particle agglomerates as opposed to the primary crystallites. This difference is probably due to the authors not employing a calcination stage, allowing for diffusion, prior to consolidation. As the relative density increased to approximately 80 % (**Figures 5c-d**), the Co film remained present around all grain boundaries as a continuous network, although the dopant concentration at the boundary cores is shown to decrease. The grain boundary Co concentration is then shown to decrease further in $2CoCGO_{90\%}$ without there being any evident change in the boundary layer thickness (**Figure 5e-f**).

This information is summarised graphically in **Figure 6** which depicts the variation in Co concentration across the grain boundary as density increases. The evaluated regions are

denoted by the green markers in the high angle annular dark field (HAADF) images, where the length of the box indicates the integration width. The width of the Co distribution is seen to have a full width half maximum (FWHM) of approximately 1.5 nm, which is more than an order of magnitude greater than the electron beam incident diameter. This could indicate the true width of the Co distribution, or be an artefact of broadening of the electron beam by scattering in the specimen. The broadening due to scattering was estimated using the results of Doig *et al*. [28] who estimated the full width at one tenth maximum (FWTM) as 78 nm in a 300 nm thick Fe specimen using a 10 nm incident beam at 100 keV. Since the densities of Fe and CGO are not too dissimilar and the beam spreading is proportional to $t^{1.5}/E$ (where t is the foil thickness and E is the electron energy) then for our 80 nm thick foils, the FWTM is estimated to be 3.53 nm, which corresponds to a FWHM of 1.77 nm. For our range of foil thicknesses (60-100 nm), the range of FWHMs for the grain boundary analysis is estimated to be 1.2-2.6 nm. Thus it can be concluded that the broadening of the Co distribution is mainly an artefact of electron beam spreading and that the true segregation width could be smaller than the one measured.

At ~70 % relative density, the grain boundary Co concentration was measured as ~4 mass %, decreasing to a bulk concentration of ~0.6 mass % beyond approximately 1 nm from the boundary core. This segregation is believed to result from the low solubility of Co within the CGO bulk lattice [29]. Increasing the sintering temperature to 881 °C reduced the grain boundary Co concentration to ~3.5 mass %. In $2CoCGO_{90\%}$, the grain boundary Co concentration decreased further to ~2.5 mass % whilst the bulk concentration remained at ~0.6 mass %. This suggests that the solubility of Co within CGO does not increase between ~850-930 °C, which is in agreement with the findings of Lewis *et al*. [30]. The variation in the Ce and Gd peak concentrations at these grain boundaries is summarised in **Table 2**. In each specimen, notable grain boundary Ce depletion and Gd enrichment are observed, but no

trend in the compositional variation of these elements was found with increasing density. After sintering to full density (1020 °C for 45 minutes), newly formed precipitates, approximately 60 nm in diameter, were observed in the 2CoCGO microstructure (**Figure 7**). EDX spectrum imaging revealed these precipitates to be both Co enriched (up to ~19 mass %) and Ce deficient. Precipitate formation will result from Co grain boundary diffusion towards triple grain junctions where the second phase crystallites will nucleate; this explains the decrease in Co concentration at the grain boundaries with increasing density and has been shown to occur increasingly with sintering temperature and time elsewhere [25]. Co enrichment (+0.7 mass % over the bulk concentration) is still observable along all grain boundaries in the fully sintered microstructure. Since the thickness of the grain boundary layer has remained constant, most of the Co that was earlier at the grain boundaries will eventually be located in these precipitates. Similar grain boundary layers have previously been reported in fully dense 2CoCGO20 [12, 27], however, the presence of a continuous Co network along all grain boundaries has not been observed before. The high density 2CoCGO sample again shows both grain boundary Gd enrichment and Ce depletion (see **Table 2**) as was observed at lower densities. Such segregation effects have been reported elsewhere in the literature by techniques including low energy ion scattering (LEIS) [31] and EELS [32] in undoped CGO. The segregation of Gd to the grain boundary probably results from the driving force to reduce lattice strain. The results also appear to indicate a decrease in Co segregation with an increase in temperature. These specimens are, however, not at equilibrium since the different temperatures correspond to different degrees of densification, and since the segregated Co is being depleted in the later stages of sintering by the formation of second phase precipitates.

Figure 8 shows EELS spectra obtained from the O-K edge and Co-L edges within and adjacent to a Co-rich precipitate. The spectra indicate that the Co concentration outside

the precipitates is below the limit of detection of the technique (~0.5 atomic % [24]); this is consistent with the EDX spectrum imaging results. A comparison between the energy loss near edge spectroscopy (ELNES) features and those from standard literature spectra [33, 34] reveals that the Co-precipitates are Co_3O_4-like in nature. These results, however, differ from those of Zhang *et al*. [25], who concluded that the Co precipitates formed in 2CoCGO20 were CoO-like in nature. It is likely that this disparity results from the air-quenched cooling method used by Zhang *et al*., which might retain the high temperature phase down to room temperature.

3.2.2 Cr-dopant Distribution as a Function of Density

The location and concentration of the Cr oxide dopant was similarly recorded as a function of relative density in 2CrCGO. These results are illustrated in **Figure 9**. At approximately 70 % relative density ($2CrCGO_{70\%}$), significant Cr enrichment is observed around all primary crystallite grain boundaries as was the case with Co. As the relative density is increased to approximately 80 % (**Figure 9c and d**), Cr segregation is again shown along all grain boundaries, although at this density, the dopant concentration at the boundary core has decreased. Since there is no considerable change in layer thickness, an increase in dopant diffusion to the triple junctions is suspected to have occurred as with Co. In $2CrCGO_{90\%}$ (**Figure 9e and f**), another significant drop in the grain boundary Cr concentration is observed, presumably resulting from further diffusion to the triple junctions.

This information is summarised graphically in **Figure 10** which depicts the variation in Cr concentration across the grain boundary as the density increased. At 70 % relative density, the grain boundary core Cr concentration was measured at ~5.9 mass %, decreasing to a bulk concentration of ~2.5 mass % after ~1 nm. As was discussed previously with Co

segregation, the width of the Cr distribution is mainly due to electron beam broadening. The grain boundary concentration is then shown to decrease to ~5 mass % in $2CrCGO_{80\%}$. The difference shown in the bulk Cr concentration on either side of the boundary in **Figure 10** probably results from a difference in grain inclination between the grains in the thin specimen thereby creating different interaction volumes in the two grains. As the relative density approaches 90 %, the grain boundary Cr concentration again decreases to ~3 mass % (+1.2 mass % above the bulk concentration). The variation in the Ce and Gd concentrations across the same grain boundary regions are summarised in **Table 3**. Each specimen again exhibits enhanced grain boundary Gd enrichment and Ce depletion, with this effect becoming more pronounced with increasing relative density. A maximum relative density of ~96 % was achieved in 2CrCGO after sintering at 1500 °C for 5 hours. At this relative density, residual Cr enrichment (+0.3 mass % over the bulk concentration) is observed across the grain boundary region, with an increased width of approximately 10 nm. Similarly, the width of the grain boundary Gd enriched region (+4.7 mass % over bulk concentration) and Ce depletion region (-7.5 mass % under bulk concentration) also appear to have increased under these sintering conditions. EDX spectrum imaging also reveals the presence of a second phase within the high density microstructure (**Figure 11**) existing as isolated grains ranging from approximately 200-400 nm in diameter. This phase is shown to be both Gd and Cr enriched throughout (~50 and ~20 mass % respectively).

It is proposed that at ~70 % relative density, an enhancement in grain boundary Gd segregation (above that seen in undoped CGO [31, 32]) will occur, providing the concentration of Gd and Cr necessary for the formation of this second phase. With increasing sintering temperature and time, both Cr and Gd will diffuse along the grain boundary to the triple junction regions where second phase precipitates will nucleate (resulting in both a decreased grain boundary and bulk Cr concentration). Given the limited overall concentration

of Cr within the system, grain boundary Gd excess will remain after the formation of this second phase, although it is possible that at elevated temperatures some Gd will diffuse back into the bulk. The microstructural evolution described above is consistent with the chemical analysis summarised in **Table 3**.

Figure 12 shows EELS spectra obtained from the O-K edge and Cr-L edges both within and adjacent to a second phase precipitate in the high density 2CrCGO microstructure. The spectra again indicate that the Cr concentration outside the precipitate is below the limit of detection. Unambiguous determination of the Cr valence state proved difficult due to similarities in the fine structures of several Cr oxides. Difficulty in distinguishing Cr^{3+} from Cr^{4+} using EELS has previously been reported [35]. A comparison of the ELNES features with those from standard literature spectra [36] did however reveal fine structures that were most similar to those of CrO_2, suggesting the presence of Cr^{4+} in the precipitates.

3.3 Mechanisms for Modified Sintering Behaviour

The rate of densification in a ceramic is the combination of both a driving force and the transport of material in response to this driving force and, in principle, TMO additions could affect either, or both of these factors. The driving force for densification is a reduction in the total excess energy associated with the surface area. Thus impurity segregation at surfaces could increase or decrease the surface energy per unit area, which would increase or decrease the driving force for densification respectively. However, it is unlikely that this could account for the large differences in densification rates caused by the TMO dopants and therefore the transport processes are probably more affected.

The transport process controlling densification is most likely grain boundary diffusion. In a ceramic, all elemental components must move together and the overall

transport rate is controlled by the slowest species. In the case of doped ceria, this is likely to be Ce^{4+} since it has the highest charge and therefore the strongest interactions with the surrounding ions.

Grain boundaries in fast ion conductors are known to have a complicated structure with an electrically charged core and narrow space charge regions of opposite charge extending a short distance on either side of the core. Hojo *et al*. [37] studied the structure of a symmetrical tilt boundary in undoped ceria and found it to have an oxygen deficient core approximately 0.5 nm wide. Lei *et al*. [32] studied the structure and composition of a symmetrical tilt boundary in yttria-stabilised zirconia (YSZ) and found it to be similar to the ceria grain boundary with an oxygen deficient core and a structural width of approximately 0.5 nm. Although Y was segregated to the boundary core, it was insufficient to compensate the charge of the oxygen deficiency with the result being that the core had a net positive charge. The authors also observed qualitatively similar segregation in boundaries of CGO polycrystalline ceramics. Jasper *et al*. [38] also studied grain boundaries in CGO ceramics and observed structural boundary widths in the range 1.4-2.9 nm. In acceptor-doped fluorite-structured oxygen ion conductors there is thus strong evidence that the core has a structural width of 0.5-2 nm and carries a net positive charge that is surrounded by a negative space charge with a total width of approximately 4 nm [39, 40]. The core positive charge is due to an excess of cation charge over the stoichiometric value and could be regarded as either cation excess or oxygen deficiency. It has already been established that Gd is segregated to the grain boundaries in CGO and, if Gd^{3+} replaces Ce^{4+}, then a negative core charge would result. Therefore, the positive core charge can be regarded as a segregation of oxygen vacancies to the core which results in over-compensation of the effective negative charge of the Gd. In other words, the segregation of oxygen vacancies to the core is energetically more

favourable than the segregation of Gd ions. The compensating negative space charge is due to a depletion of oxygen lattice vacancies which have effective positive charge.

Since Ce diffusion in the lattice is so slow, it is unlikely that the Ce grain boundary transport controlling densification takes place by enhanced cation defect concentrations in the space charge regions. It is far more likely that Ce grain boundary diffusion is dominated by the boundary core and therefore we consider how this might be influenced by the TMOs.

As outlined in the introduction, the enhanced densification in Co-doped CGO has previously been attributed to a grain boundary "liquid phase" film with a eutectic CeO_2-CoO liquidus temperature that is much lower than the bulk eutectic temperature. The present analytical results show a grain boundary Co/Ce ratio of 4:64 by mass at ~70 % relative density. Neglecting the Gd content, this corresponds to a composition of 13 mol % CoO and 87 mol % CeO_2. This is similar to the eutectic composition predicted by Ivas *et al*. [19] for 5 nm CoO-CeO_2 nano-particles. Our results indicate that the width of the segregated Co layer is less than 3 nm and probably of a similar dimension to the boundary core. At such small dimensions it is probably not meaningful to regard the boundary as a separate liquid phase, nevertheless it has different composition, structure and properties to the bulk lattice. The present observations for the beneficial effect of Co are thus not inconsistent with the concept of a grain boundary core structure that is "quasi-liquid" (i.e. highly disordered) in which Ce diffusion is enhanced. However, the present experimental results of the grain boundary compositional changes show that qualitatively both Co and Cr behave in a similar way, but yet have very different effects on densification rate and, by implication, the transport of Ce in the boundary cores. No data were found for the ceria-chromia phase diagram, but an evaluation is available for Ce_2O_3 –Al_2O_3 [41] which shows a eutectic composition of 25 mol % alumina melting at 1725 °C Since this temperature is not much higher than that of the CeO_2-CoO eutectic (1644 °C), it seems unlikely that the "quasi-liquid" core model can

account for the opposing effects of Co and Cr . Core structures of grain boundaries in doped ceramics can be very complicated and can undergo significant structural rearrangements known as complexions [42, 43]. For example, the formation of disordered liquid-like structures at grain boundaries has been shown to explain activated sub-solidus sintering in tungsten alloys [J. Luo and X. Shi, Applied Physics Letters 92, 101901 (2008).] and in Bi-doped ZnO varistor ceramics [Y.-M. Chiang, H. Wang and J.-R. Lee, Journal of Microscopy 191 (3), 275-285 (1998)]. It is therefore possible that similar phenomena could explain the different effects of Co and Cr, but in the following we consider an alternative explanation.

One significant difference between Co and Cr from the results of the present study is the difference in ionic charge: 2+ for Co, but 4+ for Cr. Thus when the ions segregate to the boundary cores, they will have a different influence on the segregation of Gd and the core charge. We speculate that the modification of the boundary cores by the different charges of the Co or Cr ions leads to a different effect on the concentration and mobility of defects by which the Ce ions diffuse within the core regions.

The exact mechanism by which this occurs cannot be deduced from the current results. It is however speculated that the lower ionic charge of Co reduces the positive core charge. As a result, the oxygen vacancy concentration in the core is also reduced. In principle it is not strictly valid to identify point defects and their equilibria in the boundary cores because there is no fixed ideal atomic arrangement as in the crystal lattice. Nevertheless, there should be some comparable concepts and relationships because the fundamental chemical bonding in the material is preserved even at the boundaries. In the crystal lattice, the Schottky equilibrium requires that a decrease in the concentration of oxygen vacancies would lead to an increase in the concentration of Ce vacancies, and a similar relationship might be expected in the boundary core. In addition, the lowering of the positive core charge would reduce the electrostatic interaction with the Ce^{4+} ions making it

easier for them to move. Thus the segregation of Co to the boundary core would increase the mobility of Ce in the core and enhance densification. Pure Co-oxide is also known to undergo a phase transition (Co_3O_4 to CoO) at approximately 900 ºC [44]. The reduction of $Co^{3+/2+}$ to Co^{2+} will further reduce the positive charge associated with the grain boundary core and further reduce the concentration of oxygen vacancies in the core. The temperature of this reduction process is in good agreement with that of the maximum shrinkage rate shown in 2CoCGO (**Figure 1**).

The opposite would be the case for Cr. The segregation of Cr would increase the positive charge at the boundary core and increase the concentration of vacant oxygen sites within the core. This would suppress the concentration of Ce vacancies whilst the increased positive core charge would reduce the Ce ion mobility thereby reducing the grain boundary diffusivity of Ce, retarding densification. A schematic illustrating these mechanisms is shown for both Co- and Cr-doped CGO in **Figure 13**. In a later paper we will present experimental evidence showing that these effects on core charge are also consistent with the effect of Co and Cr on oxygen ionic conductivity across CGO grain boundaries.

It is finally worth mentioning that changes in grain boundary structure, complexions and core charges are not mutually exclusive and the actual effects of the TMOs will probably include contributions from them all.

4. Conclusions

The effects of two contrasting TMO dopants on the densification of CGO have been examined. Whilst low concentration Co oxide addition has been shown to improve the sintering kinetics, the addition of Cr oxide at concentrations greater than 0.1 cat % has been shown to inhibit the sinterabilty of the material. Measurements of the apparent sintering

activation energy revealed that Co-doping reduced the activation energy required for densification whilst Cr-doping significantly increased it. EDX spectrum imaging in high resolution STEM was used to examine the location and concentration of the dopants in 2CoCGO and 2CrCGO as a function of relative density. With increasing density, the concentration of Co at the grain boundary was found to decrease. This corresponded to the formation of Co_3O_4 precipitates (observed after slow cooling) at the triple grain junctions. Similar conclusions were also drawn from the Cr-doped specimens; with the concentration of Cr at the grain boundary shown to decrease with increasing relative density. EDX spectrum imaging and subsequent EELS measurements of fully dense 2CrCGO revealed the presence of precipitates containing Cr^{4+} and Gd which formed via the diffusion of the species along the grain boundary during sintering. The improved densification kinetics observed in Co-doped CGO are suggested to result from enhanced solid-state diffusion, resulting from the reduction of the transition metal oxidation state at approximately 900 °C. It is proposed that the resulting reduction in positive charge at the grain boundary core modifies the concentrations of Gd, oxygen vacancies and Ce vacancies in the core leading to enhanced grain boundary Ce diffusion and an enhancement in densification. The inhibiting effects of Cr addition are suggested to be by a similar mechanism, but with opposite effects, resulting from the higher charge of the Cr^{4+} ion increasing the positive charge on the boundary core.

5. Acknowledgements

The authors would like to thank the EPSRC and Ceres Power Limited who funded this work in the form of a CASE award.

6. References

[1] Etsell TH, Flengas SN. Chemical Reviews 1970;70:339.

[2] Inaba H, Tagawa H. Solid State Ionics 1996;83:1.

[3] Mogensen M, Sammes NM, Tompsett GA. Solid State Ionics 2000;129:63.

[4] Steele BCH. Solid State Ionics 2000;129:95.

[5] Inaba H, Nakajima T, Tagawa H. Solid State Ionics 1998;106:263.

[6] Zhang T, Kong L, Zeng Z, Huang H, Hing P, Xia Z, Kilner J. J Solid State Electrochem 2003;7:348.

[7] Fuentes RO, Baker RT. International Journal of Hydrogen Energy 2008;33:3480.

[8] Cheng J-G, Zha S-W, Huang J, Liu X-Q, Meng G-Y. Materials Chemistry and Physics 2003;78:791.

[9] Moure A, Tartaj J, Moure C. Journal of the American Ceramic Society 2009;92:2197.

[10] Chen P-L, Chen IW. Journal of the American Ceramic Society 1996;79:3129.

[11] Hao X, Liu Y, Wang Z, Qiao J, Sun K. Journal of Power Sources 2012;210:86.

[12] Kleinlogel C, Gauckler LJ. Advanced Materials 2001;13:1081.

[13] Kleinlogel C, Gauckler LJ. Solid State Ionics 2000;135:567.

[14] Zhang TS, Ma J, Kong LB, Chan SH, Hing P, Kilner JA. Solid State Ionics 2004;167:203.

[15] Aguadero A, Fawcett L, Taub S, Woolley R, Wu K-T, Xu N, Kilner J, Skinner S. Journal of Materials Science 2012;47:3925.

[16] Kleinlogel CM, Gauckler* LJ. Journal of Electroceramics 2000;5:231.

[17] Fagg DP, Abrantes JCC, Pérez-Coll D, Núñez P, Kharton VV, Frade JR. Electrochimica Acta 2003;48:1023.

[18] Lewis GS, Atkinson A, Steele BCH. Sintering of Gadolina-Doped Ceria at Reduced Temperature. In: Bossel U, editor. Fourth European Solid Oxide Fuel Cell Forum. Oberrohrdorf, Switzerland, 2000. p. 773.

[19] Ivas T, Grundy AN, Povoden-Karadeniz E, Gauckler LJ. Calphad 2012;36:57.

[20] Tianshu Z, Hing P, Huang H, Kilner J. Journal of Materials Science 2002;37:997.

[21] Zhang TS, Ma J, Leng YJ, Chan SH, Hing P, Kilner JA. Solid State Ionics 2004;168:187.

[22] Taub S, Wang X, Kilner JA, Atkinson A. The Effect of Transition Metal Dopants on the Sintering and Electrical Properties of Cerium Gadolinium Oxide. In: Lefebvre-Joud F, Bouyer E, Kiviaho J, Laurencin J, Le Naour F, Mougin J, Petitjean M, editors. 10th European SOFC Forum, vol. Chapter 16. Lurcern, Switzerland, 2012. p.50.

[23] Jud E, Zhang Z, Sigle W, Gauckler L. Journal of Electroceramics 2006;16:191.

[24] Avila-Paredes HJ, Kim S. Solid State Ionics 2006;177:3075.

[25] Zhang Z, Sigle W, Rühle M, Jud E, Gauckler LJ. Acta Materialia 2007;55:2907.

[26] Zając W, Suescun L, Świerczek K, Molenda J. Journal of Power Sources 2009;194:2.

[27] Jud E, Huwiler CB, Gauckler LJ. Journal of the American Ceramic Society 2005;88:3013.

[28] Doig P, Flewitt PEJ. Scripta Metallurgica 1984;18:561.

[29] Sirman JD, Waller D, Kilner JA. Electrochemical Society Proceedings 1997;97-18:1159.

[30] Lewis GS, Atkinson A, Steele BCH, Drennan J. Solid State Ionics 2002;152–153:567.

[31] Scanlon PJ, Bink RAM, van Berkel FPF, Christie GM, van Ijzendoorn LJ, Brongersma HH, van Welzenis RG. Solid State Ionics 1998;112:123.

[32] Lei Y, Ito Y, Browning ND, Mazanec TJ. Journal of the American Ceramic Society 2002;85:2359.

[33] Zhang Z. Ultramicroscopy 2007;107:598.

[34] Zhao Y, Feltes TE, Regalbuto JR, Meyer RJ, Klie RF. Journal of Applied Physics 2010;108:063704.

[35] Daulton TL, Little BJ. Ultramicroscopy 2006;106:561.

[36] Suzuki S, Tomita M. Japanese Journal of Applied Physics 1997;36:4341.

[37] Hojo H, Mizoguchi T, Ohta H, Findlay SD, Shibata N, Yamamoto T, Ikuhara Y. Nano Letters 2010;10:4668.

[38] Jasper A, Kilner JA, McComb DW. Solid State Ionics 2008;179:904.

[39] Guo X, Waser R. Progress in Materials Science 2006;51:151.

[40] Guo X, Sigle W, Maier J. Journal of the American Ceramic Society 2003;86:77.

[41] Wu P, Pelton AD. Journal of Alloys and Compounds 1992;179:259.

[42] Dillon SJ, Harmer MP. Journal of the European Ceramic Society 2008;28:1485.

[43] Cantwell PR, Tang M, Dillon SJ, Luo J, Rohrer GS, Harmer MP. Acta Materialia 2014;62:1.

[44] Mocala K, Navrotsky A, Sherman DM. Phys Chem Minerals 1992;19:88.

List of Figures

Figure 1 - Density as a function of temperature in constant heating rate dilatometry (10 °C min^{-1}) for undoped CGO and 2 cat % Co-doped CGO (2CoCGO). The solid and dashed lines represent the relative linear shrinkage rates of CGO and 2CoCGO as a function of temperature respectively.

Figure 2 – Constant heating rate dilatometry of Cr-doped CGO samples performed at 10 °C min^{-1} **(a)** Relative density as a function of temperature **(b)** Relative linear shrinkage as a function of temperature.

Figure 3 – Apparent sintering activation energy as a function of relative density determined from constant heating rate dilatometry.

Figure 4 – TEM micrographs of **(a)** CGO **(b)** 2CoCGO and **(c)** 2CrCGO sintered to 932 °C (without dwell time) at 10 °C min^{-1}.

Figure 5 – Co distribution as a function of relative density. **(a, c, e)** HAADF images of 2CoCGO at approximately 70, 80 and 90 % relative density respectively **(b, d, f)** Quantified Co spectrum images (normalised mass %) corresponding to figures 5a, c and e. The markers on figures 5a, c and e indicate the location of the line scans depicted in figure 6.

Figure 6 – Quantified Co line profiles across a grain boundary region in $2CoCGO_{70\%}$, $2CoCGO_{80\%}$ and $2CoCGO_{90\%}$. All values are expressed in normalised mass %. For clarity, error bars are only shown for every other data point.

Figure 7 – 2CoCGO at >99 % relative density (sintered at 1020 °C for 45 minutes) **(a)** HAADF image **(b)** Corresponding Co concentration spectrum image (normalised mass %).

Figure 8 – EELS analysis of 2CoCGO sintered at 1020 °C for 45 minutes indicating the O-K edge and Co-L edges inside and immediately adjacent to a Co-rich precipitate.

Figure 9 – Cr distribution as a function of relative density. **(a, c, e)** HAADF images of 2CrCGO at approximately 70, 80 and 90 % relative density respectively **(b, d, f)** Quantified Cr spectrum images (normalised mass %) corresponding to figures 5a, c and e. The markers on figures 5a, c and e indicate the location of the line scans depicted in figure 10.

Figure 10 – Quantified Cr line profiles across a grain boundary region in $2CrCGO_{70\%}$, $2CrCGO_{80\%}$ and $2CrCGO_{90\%}$. All values are expressed in normalised mass %.

Figure 11 – 2CrCGO sintered to 1500 °C for 5 hour (~96% relative density). (a) HAADF image (b) Combined quantified Ce+Cr map (c) Combined quantified Ce+Gd map.

Figure 12 - EELS analysis of 2CrCGO sintered at 1500°C for 5 hours indicating the O-K edge and Cr-L edges inside and immediately adjacent to a Cr-rich precipitate.

Figure 13 – Schematic illustrating the variation in defect concentrations across a grain boundary in CGO, 2CoCGO and 2CrCGO. Schematic not to scale.

List of Figures

Figure 1 - Density as a function of temperature in constant heating rate dilatometry (10 °C min^{-1}) for undoped CGO and 2 cat % Co-doped CGO (2CoCGO). The solid and dashed lines represent the relative linear shrinkage rates of CGO and 2CoCGO as a function of temperature respectively.

Figure 2 – Constant heating rate dilatometry of Cr-doped CGO samples performed at 10 °C min^{-1} **(a)** Relative density as a function of temperature **(b)** Relative linear shrinkage as a function of temperature.

Figure 3 – Apparent sintering activation energy as a function of relative density determined from constant heating rate dilatometry.

Figure 4 – TEM micrographs of **(a)** CGO **(b)** 2CoCGO and **(c)** 2CrCGO sintered to 932 °C (without dwell time) at 10 °C min^{-1}.

Figure 5 – Co distribution as a function of relative density. **(a, c, e)** HAADF images of 2CoCGO at approximately 70, 80 and 90 % relative density respectively **(b, d, f)** Quantified Co spectrum images (normalised mass %) corresponding to figures 5a, c and e. The markers on figures 5a, c and e indicate the location of the line scans depicted in figure 6.

Figure 6 – Quantified Co line profiles across a grain boundary region in $2CoCGO_{70\%}$, $2CoCGO_{80\%}$ and $2CoCGO_{90\%}$. All values are expressed in normalised mass %. For clarity, error bars are only shown for every other data point.

Figure 7 – 2CoCGO at >99 % relative density (sintered at 1020 °C for 45 minutes) **(a)** HAADF image **(b)** Corresponding Co concentration spectrum image (normalised mass %).

Figure 8 – EELS analysis of 2CoCGO sintered at 1020 °C for 45 minutes indicating the O-K edge and Co-L edges inside and immediately adjacent to a Co-rich precipitate.

Figure 9 – Cr distribution as a function of relative density. **(a, c, e)** HAADF images of 2CrCGO at approximately 70, 80 and 90 % relative density respectively **(b, d, f)** Quantified Cr spectrum images (normalised mass %) corresponding to figures 5a, c and e. The markers on figures 5a, c and e indicate the location of the line scans depicted in figure 10.

Figure 10 – Quantified Cr line profiles across a grain boundary region in $2CrCGO_{70\%}$, $2CrCGO_{80\%}$ and $2CrCGO_{90\%}$. All values are expressed in normalised mass %.

Figure 11 – 2CrCGO sintered to 1500 °C for 5 hour (~96% relative density). (a) HAADF image (b) Combined quantified Ce+Cr map (c) Combined quantified Ce+Gd map.

Figure 12 - EELS analysis of 2CrCGO sintered at 1500°C for 5 hours indicating the O-K edge and Cr-L edges inside and immediately adjacent to a Cr-rich precipitate.

Figure 13 – Schematic illustrating the variation in defect concentrations across a grain boundary in CGO, 2CoCGO and 2CrCGO. Schematic not to scale.

Figure 1

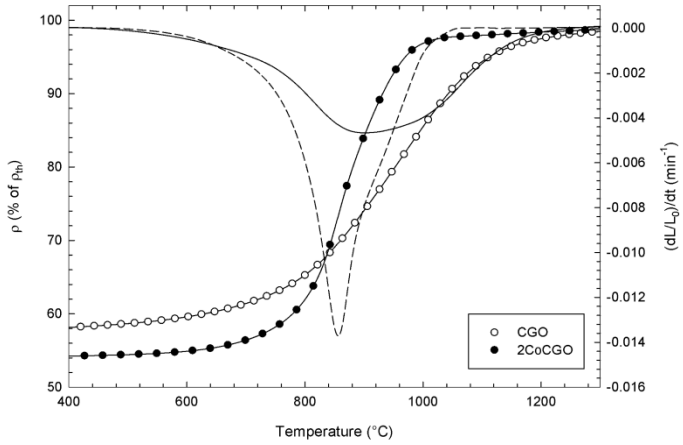

100
90
80
70
60
50
400
600
800
1000
1200
Temperature (°C)
ρ (% of ρth)
0.000
-0.002
-0.004
-0.006
-0.008
-0.010
-0.012
-0.014
-0.016
(dL/L0)/dt (min-1)
CGO
2CoCGO

Figure 2

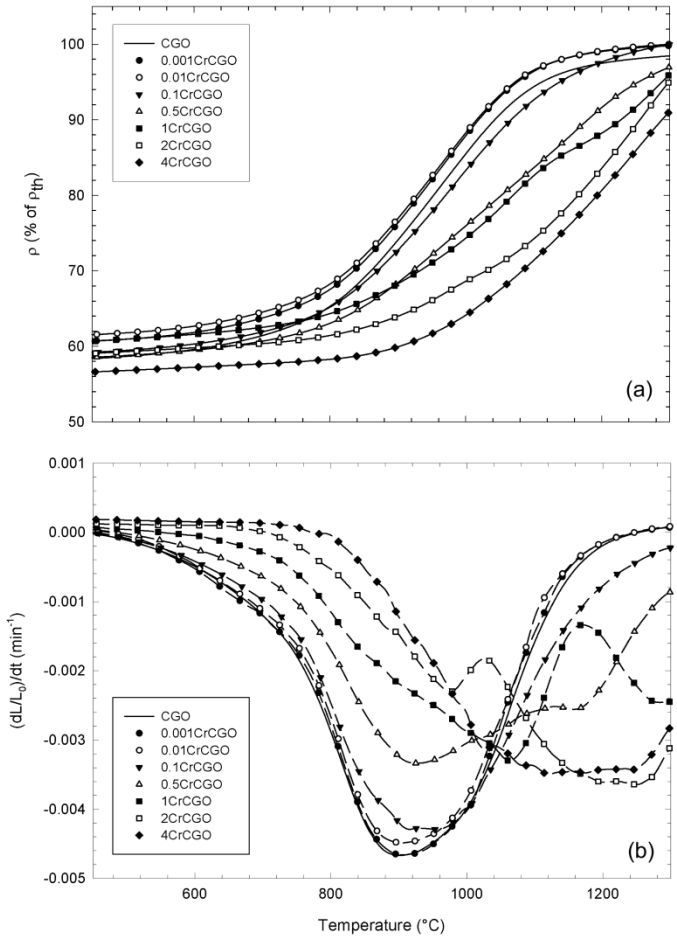

CGO
0.001CrCGO
0.01CrCGO
0.1CrCGO
0.5CrCGO
1CrCGO
2CrCGO
4CrCGO
ρ (% of ρth)
(a)
(dL/L0)/dt (min-1)
(b)
Temperature (°C)

Figure 3

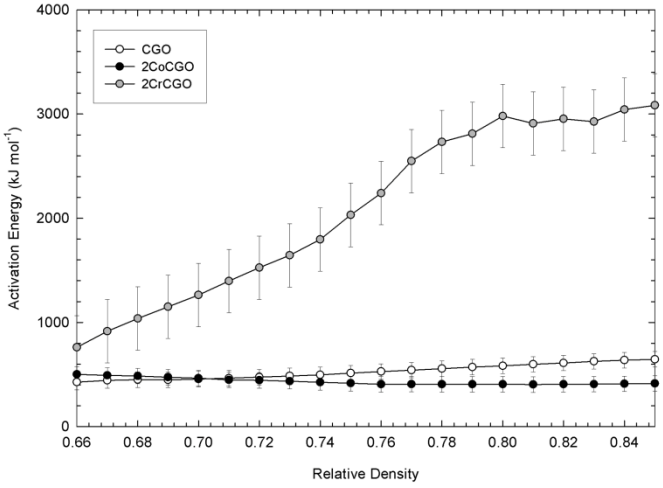

CGO
2CoCGO
2CrCGO
Activation Energy (kJ mol-1)
Relative Density
0
1000
2000
3000
4000
0.66
0.68
0.70
0.72
0.74
0.76
0.78
0.80
0.82
0.84

Figure 4

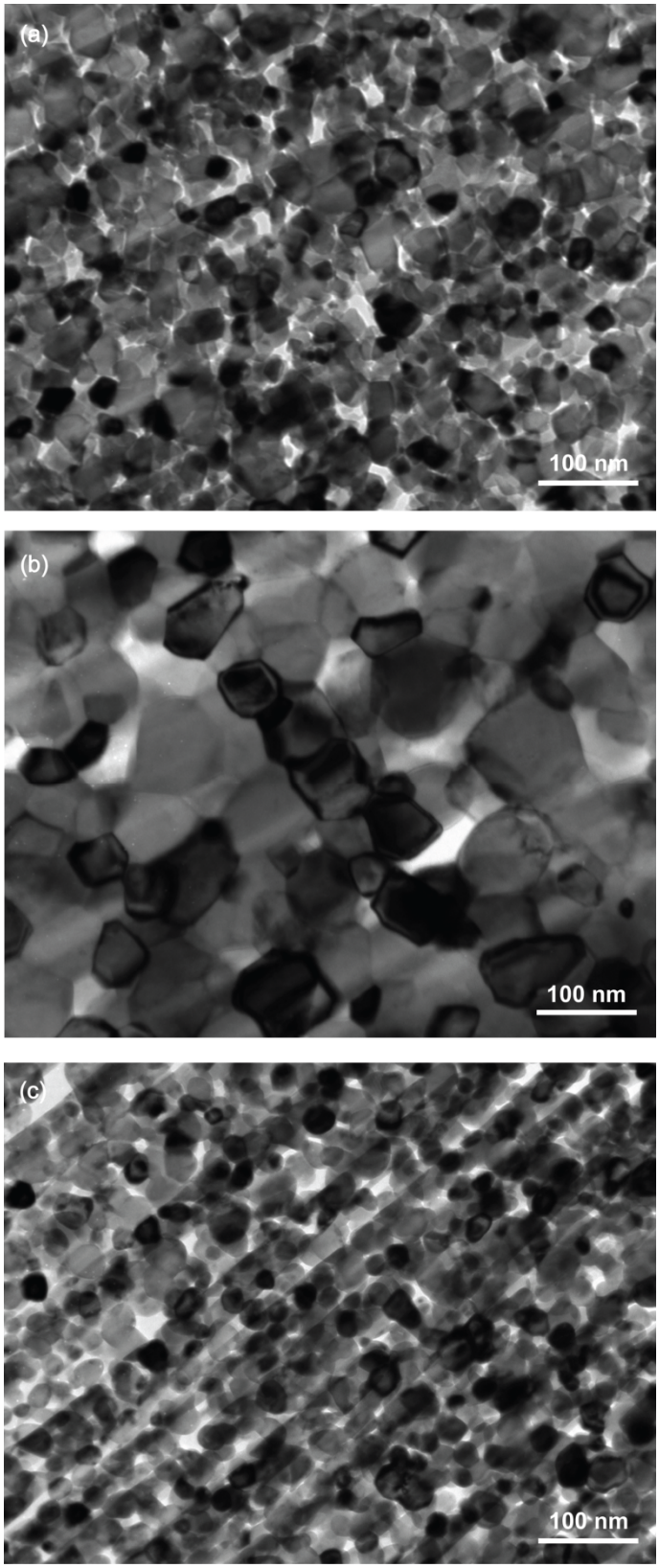


Figure 5

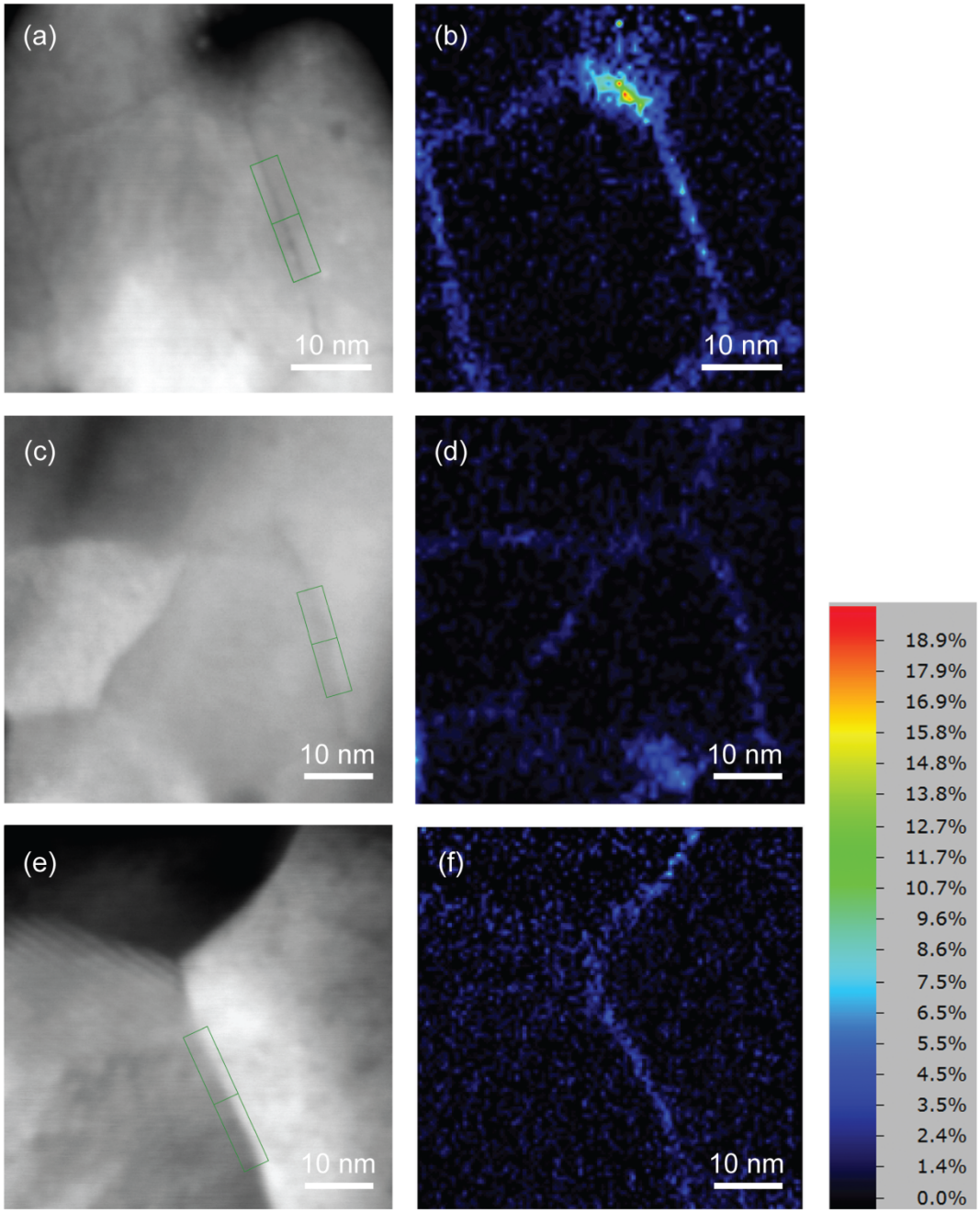

(a)
10 nm
(b)
10 nm
(c)
10 nm
(d)
10 nm
(e)
10 nm
(f)
10 nm
18.9%
17.9%
16.9%
15.8%
14.8%
13.8%
12.7%
11.7%
10.7%
9.6%
8.6%
7.5%
6.5%
5.5%
4.5%
3.5%
2.4%
1.4%
0.0%

Figure 6

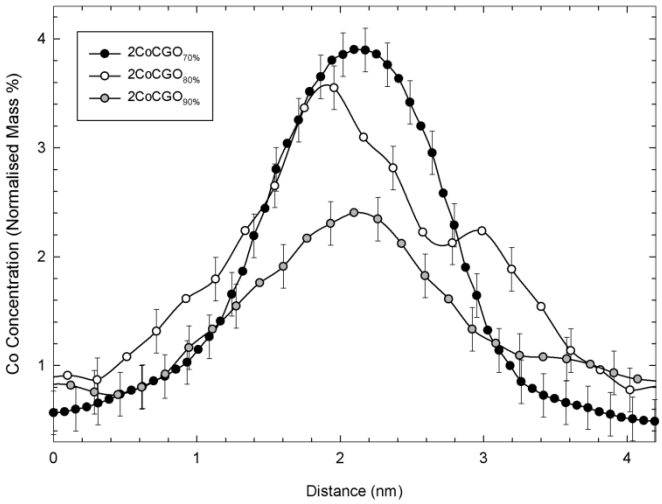

2CoCGO70%
2CoCGO80%
2CoCGO90%
Co Concentration (Normalised Mass %)
Distance (nm)
0
1
2
3
4
1
2
3
4

Figure 7

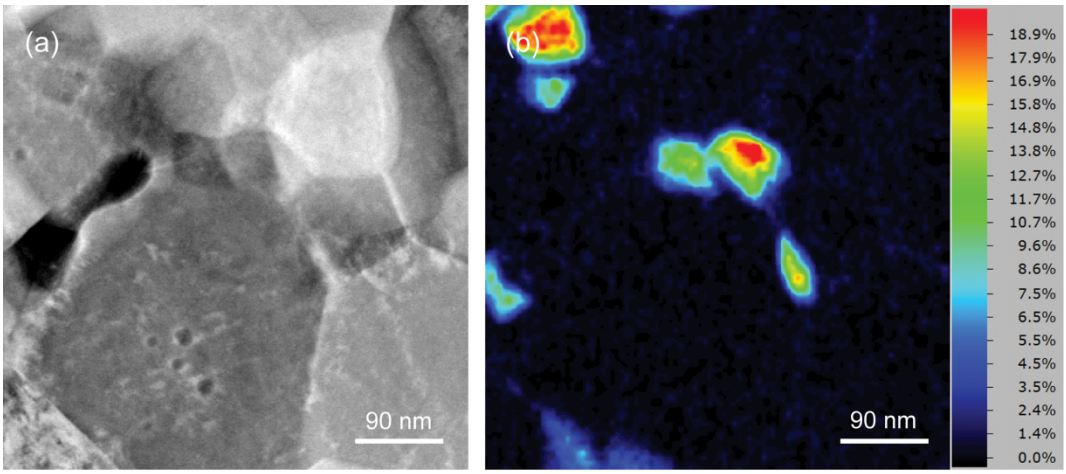

(a)
90 nm
(b)
90 nm
18.9%
17.9%
16.9%
15.8%
14.8%
13.8%
12.7%
11.7%
10.7%
9.6%
8.6%
7.5%
6.5%
5.5%
4.5%
3.5%
2.4%
1.4%
0.0%

Figure 8

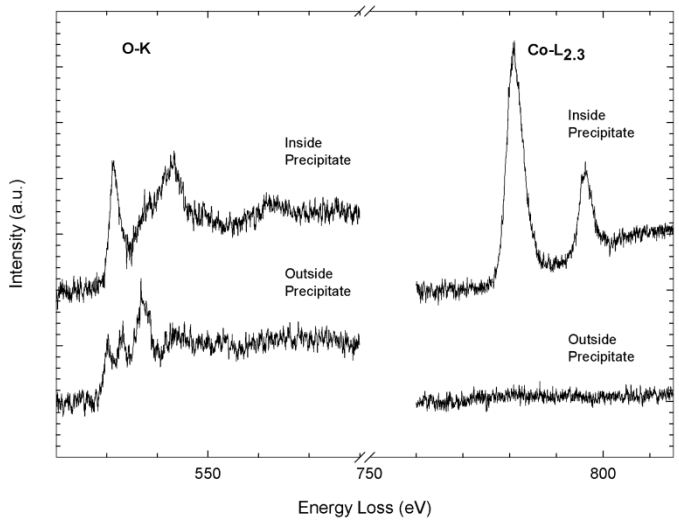

O-K
Co-L2,3
Inside
Precipitate
Outside
Precipitate
Inside
Precipitate
Outside
Precipitate
Intensity (a.u.)
550
750
800
Energy Loss (eV)

Figure 9

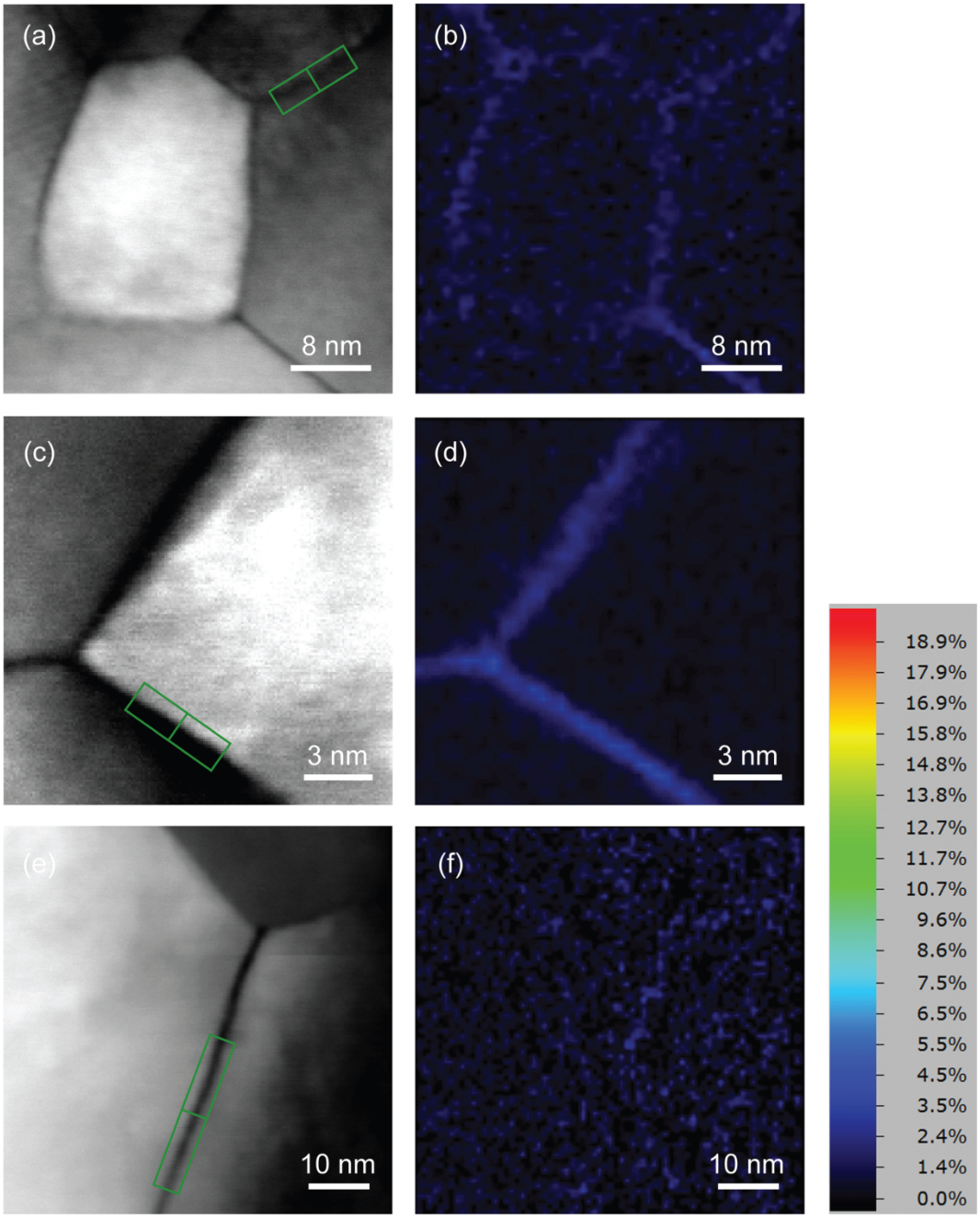

(a)
8 nm
(b)
8 nm
(c)
3 nm
(d)
3 nm
(e)
10 nm
(f)
10 nm
18.9%
17.9%
16.9%
15.8%
14.8%
13.8%
12.7%
11.7%
10.7%
9.6%
8.6%
7.5%
6.5%
5.5%
4.5%
3.5%
2.4%
1.4%
0.0%

Figure 10

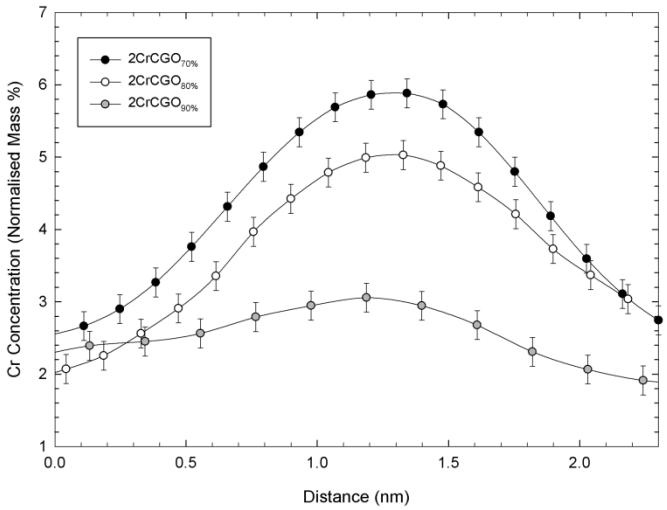

2CrCGO70%
2CrCGO80%
2CrCGO90%
Cr Concentration (Normalised Mass %)
Distance (nm)
1
2
3
4
5
6
7
0.0
0.5
1.0
1.5
2.0

Figure 11

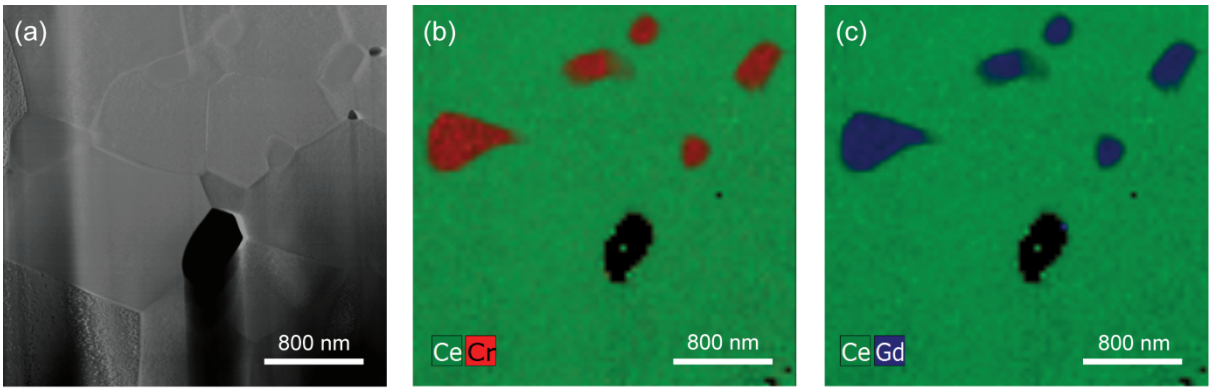


Figure 12

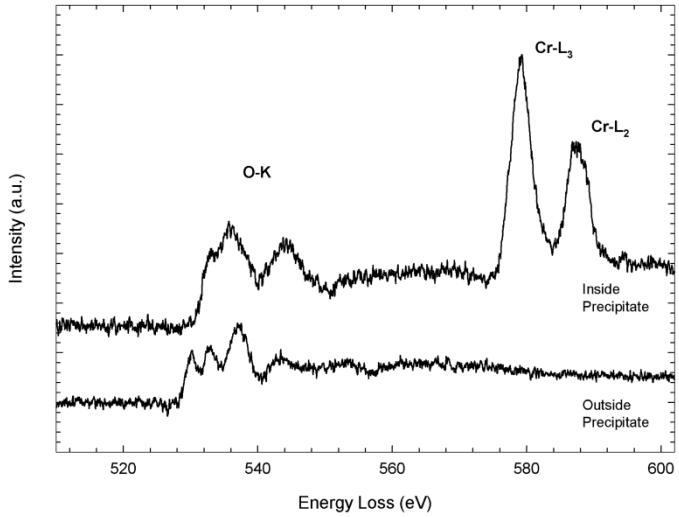
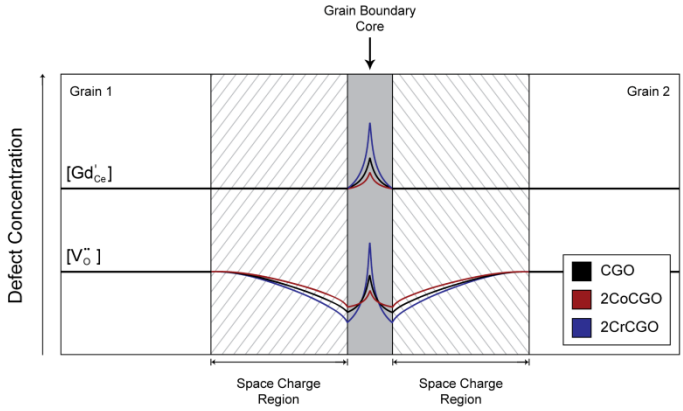

Cr-L3
Cr-L2
O-K
Inside
Precipitate
Outside
Precipitate
Intensity (a.u.)
520
540
560
580
600
Energy Loss (eV)

Figure 13


Grain Boundary
Core
Grain 1
Grain 2
Defect Concentration
$[Gd'_{Ce}]$
$[V_O^{\cdot\cdot}]$
CGO
2CoCGO
2CrCGO
Space Charge
Region
Space Charge
Region

Tables

Material	Intended Density (%)	Density Attained (%)	Sintering Temperature (°C)	Dwell Time (min)
$2CoCGO_{70\%}$	70	64.5	845	-
$2CoCGO_{80\%}$	80	73.3	881	-
$2CoCGO_{90\%}$	90	84.7	932	-
2CoCGO	100	>99	1020	45
$2CrCGO_{70\%}$	70	63.4	1030	-
$2CrCGO_{80\%}$	80	72.4	1165	-
$2CrCGO_{90\%}$	90	81.5	1256	-
2CrCGO	100	95.1	1500	300

Table 1 - Sintering conditions for samples of 2 cat % Co-doped and 2 cat % Cr-doped CGO at varying densities. Where no dwell time has been specified, the specimens were heated under constant heating rate conditions and allowed to cool slowly. 2CoCGO and 2CrCGO were sintered at heating rates of 5 °C min^{-1} with all other samples sintered at heating rates of 10 °C min^{-1}.

Material	Co (mass %)	Ce (mass %)	Gd (mass %)
$2CoCGO_{70\%}$	+3.4	-6.1	+2.2
$2CoCGO_{80\%}$	+2.9	-3.4	+1.6
$2CoCGO_{90\%}$	+1.9	-6.4	+4.7
2CoCGO	+0.7	-3.6	+2.1

Table 2 – Variation in the grain boundary composition of 2CoCGO as a function of relative density. Each values is denoted as the difference between the measured grain boundary concentration and that of the bulk. All measurements are given in normalised mass %.

Material	Cr (mass %)	Ce (mass %)	Gd (mass %)
$2CrCGO_{70\%}$	+3.4	-8.2	+3.5
$2CrCGO_{80\%}$	+2.6	-7.8	+4.6
$2CrCGO_{90\%}$	+1.2	-10	+7.9
2CrCGO	+0.3	-7.5	+4.7

Table 3 – Variation in the grain boundary composition of 2CrCGO as a function of relative density. Each values is denoted as the difference between the measured grain boundary concentration and that of the bulk. All measurements are given in normalised mass %.